Remote Sensing of Environment 315 (2024) 114411

Contents lists available at ScienceDirect

Remote Sensing of Environment

journal homepage: www.elsevier.com/locate/rse

Nearshore satellite-derived bathymetry from a single-pass satellite video: Improvements from adaptive correlation window size and modulation transfer function

Adrien N. Klotz [a,*], Rafael Almar [a], Yohan Quenet [a,b], Erwin W.J. Bergsma [c], David Youssefi [c], Stephanie Artigues [c], Nicolas Rascle [b], Boubou Aldiouma Sy [d], Abdoulaye Ndour [e]

[a] LEGOS (Univ. Toulouse, CNRS, CNES, IRD), UMR-5566, 14, Avenue Edouard Belin, 31400, Toulouse, France
[b] Laboratoire d'Océanographie Physique et Spatiale (LOPS), University of Brest, CNRS, IRD, IFREMER, 29280, Plouzané, France
[c] CNES (French Space Agency), Earth Observation Lab, 18 Avenue Edouard Belin, 31400, Toulouse, France
[d] Leidi Laboratory, Department of Geography, Territorial Dynamics and Development, Gaston Berger University (UGB), 46024, Saint-Louis, Senegal
[e] Laboratory of Sedimentology, Department of Geology, Faculty of Sciences and Technics, Cheikh Anta Diop University (UCAD), 12500, Dakar, Senegal

ARTICLE INFO

Edited by Menghua Wang

Keywords:
Bathymetry
Optical remote sensing
Temporal correlation
Satellite video
Coastal earth observations
Jilin

ABSTRACT

Accurate nearshore bathymetry estimation remains a critical challenge, impacting coastal forecasting evolution assessments through the inaccuracies in both in-situ and remote sensing surveys. This article introduces the Satellite Derived Bathymetry (SDB) temporal correlation method, showcasing its ability in deriving accurate nearshore bathymetry from one minute spaceborne videos. The approach utilises correlation of pixel intensity time series, shifted in time and space, extracted from a frame stack within a defined correlation window. The resulting correlation is then projected using the Radon Transform to infer wave characteristics (celerity and wavelength) for the estimation of depth through wave linear dispersion. Moreover, the adaptation of the correlation window based on a first wavelength estimation provided a more focused assessment of the wavefield that reveals morphological features such as sandbars in the bathymetric estimation. The method's capabilities using adapted correlation window is illustrated through its application to a metric resolution Jilin satellite video (57 s at 5 Hz) along the Saint-Louis coast in Senegal. Through this demonstration, the temporal correlation method is among the first SDB methods to successfully capture the submerged sandbar along a beach. Comparison against in-situ measurements conducted three years prior to the video acquisition shows a good agreement with a bias of 0.97 m within the initial 2 km of the cross-shore profile. Furthermore, the application of previously developed sky-glint surface elevation analysis on video pixel intensity, prior to the bathymetry estimation, significantly reduces the bias to 0.44 m in the Saint-Louis estimation. This article highlights the potential applications of future Earth observation satellite missions that will capture image sequences (or videos) such as CO3D (CNES/Airbus).

1. Introduction

Nearshore morphological change, notably concerning the bathymetry, dictates most of nearshore hydrodynamics that then influences patterns of coastline erosion/accretion. Sandy beaches often exhibit a complex arrangement of sub- and/or inter-tidal sandbars, influenced by the specific local environmental conditions, hence particular for each beach (Wijnberg and Kroon, 2002). Coastal zone evolution ranges across a broad spectrum of temporal scales, ranging from short-term due to storm events to longer-term change related to climate modes or for example the sea-level rise (Anfuso et al., 2021). These multiple temporal evolutions require long-term monitoring of the coastal zone through short and regular sampling. In addition, considering that the bathymetry is a key boundary condition of the nearshore hydrodynamic and morphodynamic process modelling, the accuracy of these models is highly dependent on the accuracy of the initial bottom boundary conditions (Sherwood et al., 2022).

In-situ nearshore bathymetry is traditionally sensed using an echo-sounder (single or multi beam) on boats, often with differential or Real Time Kinematic Global Positioning System (RTK-GPS) corrections. However, the substantial human and financial resources required to execute these surveys results in only a few coastal sites being regularly monitored. To address this limitation, coastal monitoring

* Corresponding author.
E-mail address: adrien.klotz@ird.fr (A.N. Klotz).

https://doi.org/10.1016/j.rse.2024.114411
Received 13 March 2024; Received in revised form 29 August 2024; Accepted 2 September 2024
Available online 7 September 2024

cameras and drones offer a cost-effective and flexible solution for sensing coastal environments. Unlike most in-situ measurements, the retrieval of a geophysical variable of interest requires the application of algorithms to the remotely sensed data (Holman and Haller, 2013). Over the past decades, this shift towards cost-effective solutions has accelerated the development of inversion algorithms capable of deriving bathymetry from shore-mounted cameras and Unmanned Aerial Vehicles (UAVs) offering a practical means to conduct less expensive long-term studies (Stockdon and Holman, 2000; Plant et al., 2008; Holman et al., 2013; Radermacher et al., 2014; Bergsma et al., 2016; Holman et al., 2017; Matsuba and Sato, 2018; Brodie et al., 2019; Bergsma et al., 2019c; Holman and Bergsma, 2021; Palmsten and Brodie, 2022; Rodríguez-Padilla et al., 2022; Lange et al., 2023). Also airborne LiDAR (Light Detection and Ranging) applications are being used for bathymetric surveys but require powerful computational resources (Zhou et al., 2021; Saylam et al., 2018). Although, these remote sensing approaches have emerged as effective alternatives by demonstrating their capability to derive accurate nearshore bathymetry (Wilson et al., 2014; Angnuureng et al., 2020), these solutions remain limited by their spatial coverage. Additionally, while this is slowly changing, these solutions are deployed in places where coastal communities have enough resources, leaving less developed areas without the means to protect against erosion and flooding risks (Ndour et al., 2018).

Vitousek et al. (2023) state that satellite remote sensing is transforming coastal science from a "data-poor" field into a "data-rich" field. This holds particularly true for shoreline and nearshore bathymetry measurements, as satellite-derived bathymetry (SDB) achieves unprecedented spatio-temporal coverage, enabling capturing multi-scale behaviour in coastal processes. Two separated approaches allow measurement of SDB. The first approach uses the way that light diminishes with depth in water on optical satellite acquisitions, determined by radiative transfer in the water column (Stumpf et al., 2003). This technique works well in clear non-turbid waters. The present study approach uses the wave kinematics to estimate nearshore bathymetry: it relies on how bathymetry affects waves in shallow water as wave motion is modulated in response to the water depth. Consequently, deriving the inherent characteristics of the wavefield provides a direct means of estimating the depth of the seafloor over which it propagates. This approach is developed in SDB estimation methods for optical satellite acquisitions (Abileah, 2006; Danilo and Binet, 2013; Holman et al., 2014; Poupardin et al., 2016; Bergsma et al., 2019a; de Michele et al., 2021; Bergsma et al., 2021) and Synthetic Aperture Radar (SAR) satellite acquisitions (Wiehle et al., 2019; Bian et al., 2020; Pereira et al., 2019; Mudiyanselage et al., 2024). This approach is significantly less, to hardly, affected by turbidity contrarily to the radiative approach. Such wave-based techniques obviously require waves in the observed scene (Cesbron et al., 2021). For example, Daly et al. (2022) use the wave-based *S2Shores* SDB algorithm (Almar et al., 2024) to estimate bathymetry using the 10 m resolution Sentinel-2 colour bands to estimate depths spanning over 4000 km along the West African coast. It presents a more accurate and more detailed bathymetry compared to the General Bathymetric Chart of the Oceans (GEBCO). High resolution satellites like Pléiades (CNES/Airbus) provide the possibility to capture sequences of images, up to 25 sequential images. Almar et al. (2019) estimate a SDB using the wave kinematics using 12 sequential Pléiades images by exploiting the temporal information of the acquisition using a spatio-temporal correlation technique. These Pléiades sequences presents a major challenge for spatio-temporal correlation techniques; due to the reorientation of the satellite and collection of the scene, the delay between the images is relatively long in the order of 8 s between each images. Jilin-1 Gaofen-03C satellites constellation acquire raster images (such as mobile phone cameras), referred to as frames, with a sampling period of 0.1 or 0.2 s (depending on the operator's choice). This is why their acquisitions can be qualified as spaceborne videos, even though no clear definition distinguishing sequence and video has been established so far. Recently, Almar et al. (2022) utilised a 20-second video acquisition from a Jilin-01-07 (92 cm resolution) to derive a topo-bathymetric continuum of Duck Beach, NC, USA, using spatio-temporal correlation techniques. This first encouraging demonstration of the spatio-temporal correlation approach needed to be tested and replicated for different sites and conditions.

Quantifying the relationship between remotely sensed signals and the geophysical variable of interest is a complex process. For wave observations, the optical signal captured by sensors is a proxy for the free surface slope, not the free surface itself. The optical sensors, such as cameras sense this proxy of the free surface slope through pixel intensity variations. Pixel intensity variations are related to water surface elevation through a modulation transfer function (MTF), which governs the relationship between the phases and amplitudes of the observed optical intensity variations and the true waveform. Catálan and Haller (2008) identified two distinct mechanisms governing the MTF, depending on the wave position relative to the breaking point. Before the breaking point, the MTF is primarily influenced by the specular reflection of incident light on the free surface. The main factors contributing to the MTF include: (1) The instantaneous angle defined by the light source (e.g., the sun), wave propagation direction, and sensor. Optical intensity variations decrease when the wave propagation direction is perpendicular to the bisector formed by the sun and the sensor (Catálan and Haller, 2008). (2) The relative angle between the wave propagation direction and the sensor. Optical intensity variations exhibit greater amplitude when waves propagate in the direction of the sensor's view angle and tend to diminish when waves propagate perpendicularly to the sensor's view angle (Catálan and Haller, 2008; Holman et al., 2017; Almar et al., 2019; Perugini et al., 2019). (3) Sun-glint, which occurs when sunlight is reflected directly off the sea surface (Kudryavtsev et al., 2017). (4) Sky-glint, caused by the reflection of the sky on the water surface. This reflection varies because the sky appears darker at the zenith than at the horizon, creating an intensity gradient on the water surface (Almar et al., 2021a). Glints carry information to derive wave characteristics from optical signals. For instance, Kudryavtsev et al. (2017) use sun-glint to derive wave directional spectra from Sentinel-2 data. Almar et al. (2021a) use sky-glint to derive an MTF from UAV video, enabling free surface reconstruction and significant wave height (Hs) estimation after correcting for the relative angle effect. After the breaking point, the MTF is governed by isotropic scattering from the aerated and turbulent wave roller region, commonly referred to as white foam. In this zone, the MTF is less dependent on viewing geometry (Catálan and Haller, 2008). Since the sky is not reflected in this zone, the sky-glint method used by Almar et al. (2021a) cannot be applied to reconstruct the free surface of broken waves. The breaking point marks a shift in the MTF governing mechanism due to a sudden phase shift between minimal and maximal pixel intensities (Bergsma et al., 2019b). Consequently, video-based algorithms that derive wave characteristics from the spectral domain face challenges near the surf zone as waves begin to break (Brodie et al., 2018; Oades et al., 2023; Lange et al., 2023). Capturing the sandbar lying under wave breaking with remote sensing methods remains a challenge.

In this work, we describe the temporal correlation method used to estimate a bathymetry from spaceborne videos. We also discuss latest enhancements to improve the estimation accuracy of the method. First improvement involves the introduction of a wavelength-based adaptive correlation. Notably, we applied the spatio-temporal method to a one-minute Jilin-1 video capturing the Saint-Louis coast in Senegal, demonstrating its effectiveness in identifying beach features such as the submerged sandbar. Second improvement comes from the use of surface elevation anomaly derived using the sky-glint surface elevation analysis in place of pixel intensity as input of the method where estimated bathymetry from surface elevation anomalies present a smaller bias and a more stable estimation in the zone before the breaking point.

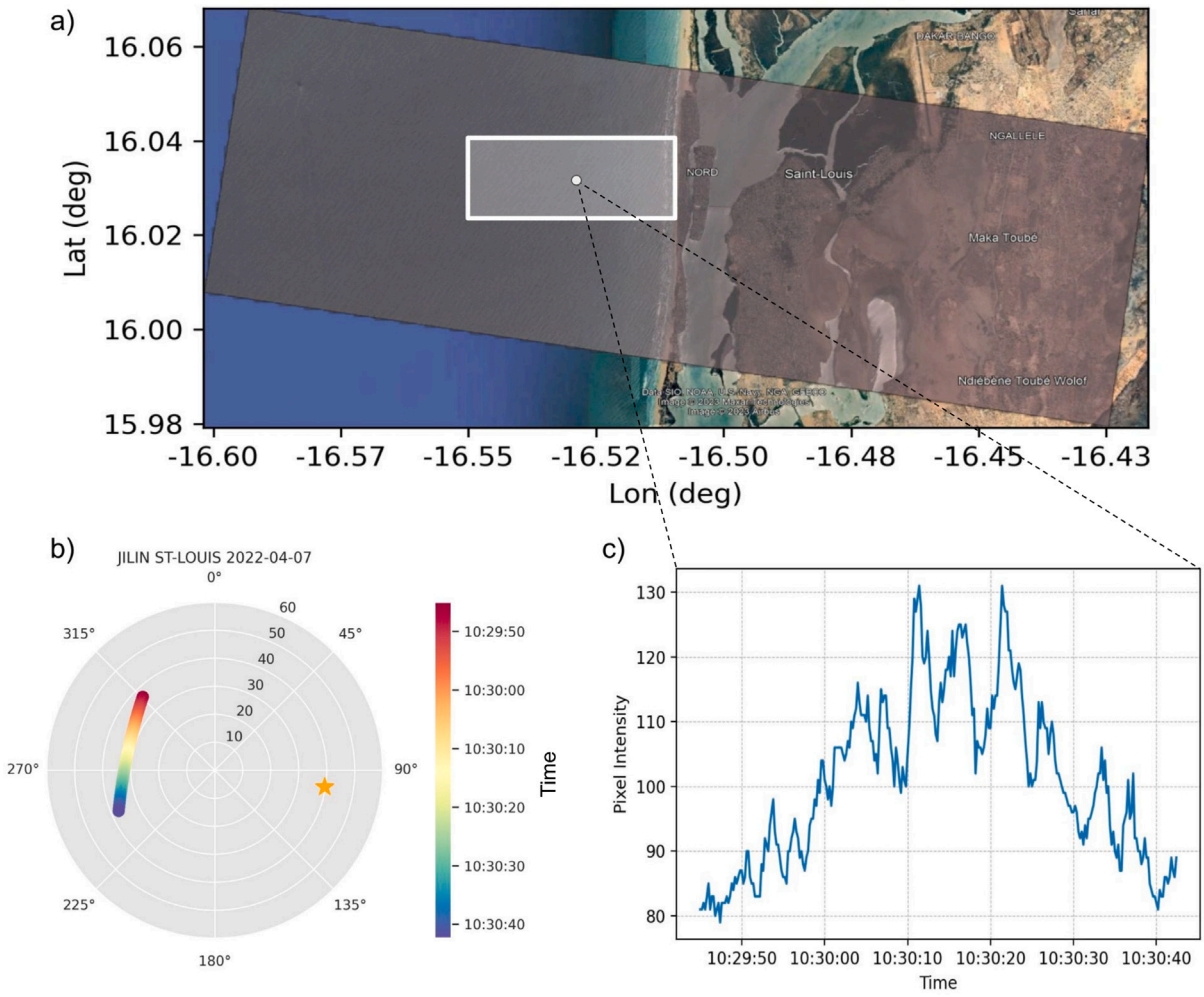

Fig. 1. (a) Frame 166 of the 288 orthorectified frames constituting the ST-LOUIS video acquisition. The light grey rectangle indicates the area analysed to derived the SDB. (b) Skyplot of Jilin-1GF03C02 Satellite trajectory during the Saint-Louis, Sénégal, 7 April 2022 video acquisition. This skyplot is centered on the Jilin image center. The angular axis (measured clockwise) represents the azimuth degrees, ranging from 0° to 359°, and the radial axis represents the zenith degrees, ranging from 0° at the zenith to 90° at the horizon. Here for clarity, the zenith degrees are limited to a range of 0° to 60°. The sun position is represented by the star. (c) Pixel intensity time-series extracted from the video. The wave signal is noticeable but it is combined with a strong "bell shape" sun glitter effect.

2. Optical video acquisitions from Jilin satellite

On April 7 2022, Jilin-1GF03C02 satellite acquired a 57 s video with an average frame rate of 5 Hz of the coast of Saint-Louis, Senegal. The video represent a total of 288 images with near metric (1.4 m) ground sampling resolution, covering an area of 130 km^2. A geometric correction and co-registration technique, currently developed by the French Space Agency CNES, employing very high-resolution Pleiades acquisitions as an on-ground reference, is employed to orthorectify the Jilin video. In Fig. 1a a geometrically corrected and orthorectified frame from the satellite video is depicted, projected on a map. At the time of the acquisition, 7 April 2022 at 10h30, sea state was characterised by a swell of peak period T_p = 7.4 s, with a significant wave height H_s = 1.4 m, coming from northwest directions at 333°, according to ERA5 climate reanalysis (Hersbach et al., 2020). These hydrodynamic conditions are close to the yearly average swell wave conditions found at Saint-Louis, Sénégal coast, namely H_s = 1.52 m, T_p = 9.23 s, northwest directions around 325° (Sadio et al., 2017). Tide elevation at the time of acquisition was −0.48 m according to FES2014 model (Lyard et al., 2021). Because the sun's position is symmetrically opposite to that of the satellite at the time of acquisition a pronounced sun glitter is observable in the satellite video (see Fig. 1b). As a consequence, at first order, the water surfaces on the video exhibit a strong rise and fall in intensity, although a wave signal remains visible (see Fig. 1c). For the purpose of this study, only a small region of the acquisition in front of the Saint-Louis village is used to derive a bathymetry and validate the proposed methodology described in the next section. This region is highlighted by the light grey rectangle in Fig. 1a.

The beach in front of Saint-Louis city is an intermediate barred microtidal beach, located in a storm-free intertropical environment. The tidal regime is semi-diurnal and the microtidal amplitude ranges from 0.5 m at neap tides to 1.6 m at spring tides. Depth-induced wave breaking over the submerged sandbar, distant of around 200 to 300 m cross-shore from the shoreline, is active at low tide. The surf zone is then defined as the region starting from the breaking point over the sandbar to the shoreline, corresponding to water depths from 0 m to 5 m (Ndour et al., 2020). In-situ bathymetric measurements were acquired in 2019 by the Shore Monitoring and Research team as part of a project coordinated by the Agence de Développement Municipal (ADM) along Saint-Louis coastline from the Mauritanian border to the far South of the Sénégal estuary. A total 264 of individual measurements inside the region of the interest in front of the Saint-Louis village were averaged alongshore to be used as a validation dataset.

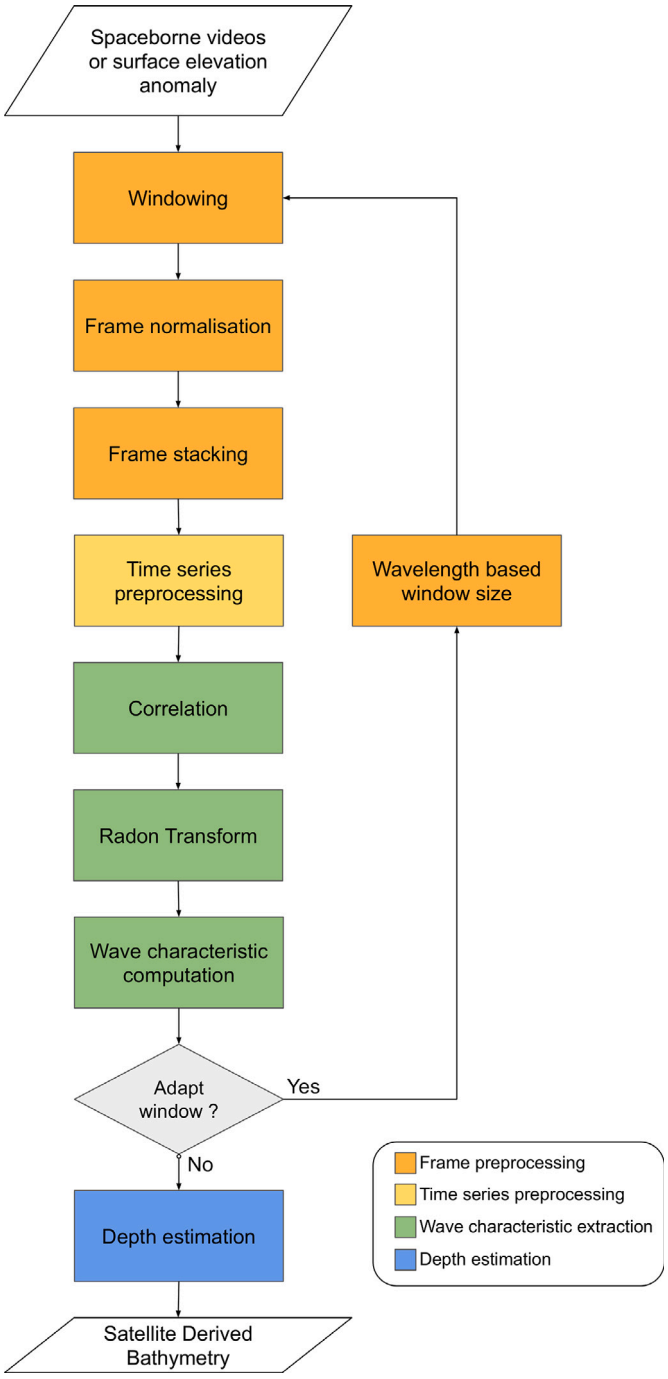

Fig. 2. Temporal correlation method's flow chart.

3. Methodology

3.1. Bathymetry inversion using temporal correlation method

In this section we describe more in detail the method presented for satellite-derived bathymetry (SDB) applications in Almar et al. (2019), along with some enhancements. The different steps involved in the temporal correlation method are shown in the flow chart in Fig. 2. Within the area of our study we arbitrarily define a regularly spaced grid where SDB is derived. To illustrate, we will walk through the process of estimating depth from a video acquisition, using one point from this grid as an example. The temporal correlation method takes the advantage of long and high temporal resolution acquisition like videos. Practically speaking, a video is seen as a dataset composed of several images, referred to as frames, captured over a specific time period. For a chosen point in the output grid, we define it as the center of a square window, hereafter called the correlation window. Within this defined window, we extract a three-dimensional spatio-temporal frame stack by cropping and stacking all frames from the video acquisition. This stack is represented by two spatial dimensions, the x and y directions, with time representing the third dimension. (See Fig. 3a.)

3.1.1. Time-series selection and pre-processing

The satellite video is a sequence of 2-dimensional optical acquisitions where discernible wave patterns are observable. Consequently, it is possible to analyse wave signals from a dataset of substantial time-series with high temporal resolution, acquired at various pixel positions within the correlation window. Each time-series is constructed along the time dimension of the frame stack by extracting values from a fixed x and y pixel position. Before stacking and extracting time-series, a normalisation is applied to each frame within the frame stack. Each pixel in the frame at position x and y the normalisation is following the equation:

$$normPixel(x,y) = \frac{Pixel(x,y) - \mu_{frame}}{std_{frame}} \quad (1)$$

where $normPixel(x,y)$ is the normalised pixel value at position x and y, $Pix(x,y)$ is the original pixel value at position x and y, μ_{frame} is the mean pixel value of the frame and std_{frame} is the standard deviation pixel value of the frame.

As presented in Fig. 3, the normalisation has removed the sun-glint from the extracted pixel intensity time-series. The sun-glint component is considered to be the mean value of the background of each frame, which varies slowly over time compared to the variation induced by the wave patterns. Frame normalisation removes this mean background, leaving only the waves in the frame. Thanks to this process, it is possible to remove the sun-glint component from the time series before applying filtering to it. Actually, not all time-series are extracted within the correlation window for computational time efficiency. A random process select the pixel positions where time-series are extracted. Although a regularly spaced grid could be utilised to select evenly distributed pixel positions within the correlation window, the randomness of the selection is crucial. This randomness is necessary to compute a spatio-temporal correlation covering a wide range of positions and, consequently, to obtain a diverse range of differential spacing between selected pixels. The correlation process is presented in the next section. In practice, although it depends on the size of the correlation window, taking into account only 15 percent of random pixel time-series is generally a good trade-off between saving computing time without altering the results compared with using all the pixel time series. Selection process is presented in Fig. 4a, 15 percent of pixels within a 100 m side-length correlation window are chosen, the chosen positions are highlighted by the red dots. The selection constructs a dataset of normalised pixel intensity time-series $I(XY_{0:P},t)$ where XY is the pixel position coordinates ranging from 0 to P, where P the number of selected pixel positions. Then, the time-series are band-pass filtered in the range 8 s to 25 s wave period to remove most of the noise that could be detrimental for the correlation process. The choice of the cut-off period values to limit the estimation error is discussed in Section 5.3.

3.1.2. Deriving wave characteristics and bathymetric inversion

Extracting wave characteristics from the time-series necessitates a combined spatial and temporal analysis. This is achieved through a correlation, where spatial and temporal information are integrated (Abessolo et al., 2020; Thuan et al., 2019; Almar et al., 2009; Bergsma

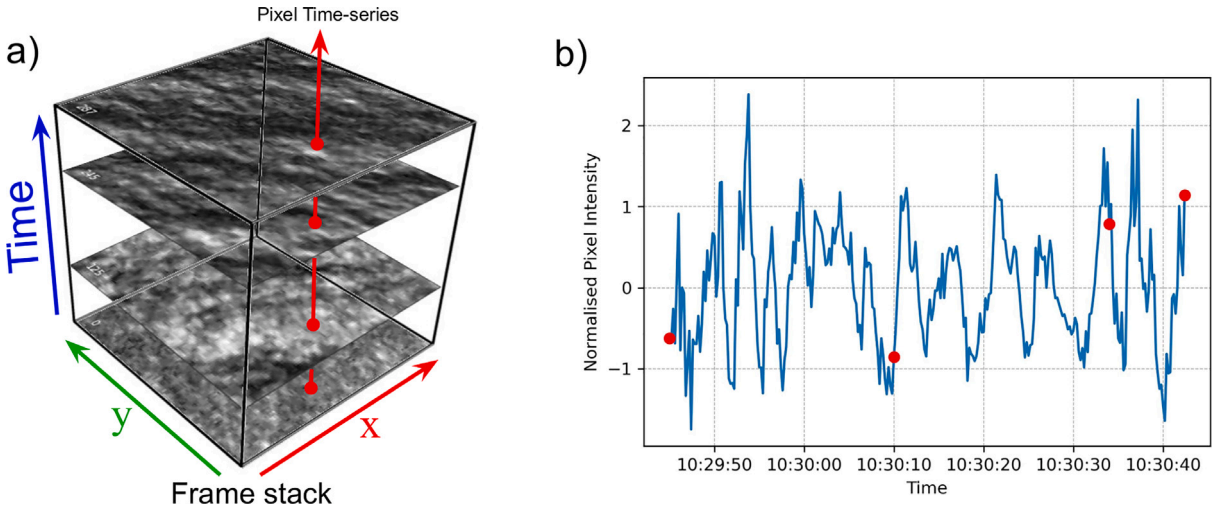

Fig. 3. (a) Frame stack example, only 4 frames of the video acquisition are displayed. The red dashed line represents a time-series extracted along the time dimension. (b) Normalised pixel intensity time-series extracted from the frame stack. The 4 red dots correspond to the time series intensity value relative to the 4 frames in the stack.

and Almar, 2018). We calculate the correlation coefficient r individually for each time-series within the dataset.

$$r(\Delta X, \Delta Y) = cor(I(XY_i, t), I(XY_j, t + \Delta t)) \tag{2}$$

where i and j are ranging from 0 to P. This involves a systematic process where we compare each individual time-series (indexed i from 0 to P) with all time-series (indexed j from 0 to P) delayed by Δt. For every pixel pair XY_i and XY_j, the spatial distances along x and y axis are computed, respectively corresponding to ΔX and ΔY coordinates into the correlation matrix. If multiple pairs of XY_i and XY_j share the same ΔX and ΔY coordinates, the result is computed as the average correlation at that specific position. As a result, this correlation explores the spatio-temporal relationships among all time series in the dataset, accounting for the influence of a time lag. The correlation the average distance covered by the waves within Δt. The value of Δt must be selected to be less than or equal to the minimum tracked wave period (Bergsma and Almar, 2018).

The correlation matrix is masked combining both a Gaussian mask, which assigns greater weight to values near the (0, 0) coordinates, and a circular mask, which is essential for the Radon Transform (RT) computation. The masked correlation matrix is transposed in the Radon (polar) space following:

$$R_r(\theta, \rho) = \iint_D r(\Delta X, \Delta Y)\delta(\rho - \Delta X \cos(\theta) - \Delta Y \sin(\theta))\, d\Delta X\, d\Delta Y \tag{3}$$

where θ, the rotational angle, is ranging from 0 to 180 degrees, δ is the Dirac delta function and ρ is the radius from the center of the correlation matrix. The wave propagation direction is derived as the maximum variance angle of the RT. Other (spectral or correlation) SDB methods make use of Radon Transform (RT) to infer wave propagation direction (Bergsma et al., 2019a, 2021; Almar et al., 2022).

The final step in deriving wave characteristics involves projecting and analysing the sinogram along the wave's propagation direction. The sinogram is expected to exhibit a damped sinusoidal pattern, with the highest peaks near $rho = 0$. The wavelength λ is calculated by averaging the distances between zero crossings and then multiplying this average by 2. The maximum peak of the sinogram allows us to quantify the wave displacement, ρ_i, over the time lag Δt, and thereby determine its celerity. However, we observe a consistent underestimation of the wave displacement, which in turn leads to an underestimation of the bathymetry. This underestimation may be due to the sensor's changing view angle during its acquisition, although further studies are necessary to confirm this hypothesis. To compensate for this underestimation, we refine ρ_i by associating a corrected wave displacement, ρ_c, with the wavelength. Specifically, ρ_c is chosen as the multiple of one-quarter of the wavelength that is closest to ρ_i. This corrected wave displacement ρ_c is used to derive the wave's phase celerity:

$$c = \frac{\rho_c}{\Delta t} \tag{4}$$

Now, wave characteristics λ, its wavelength, and c, its celerity are derived we can estimate the water depth, h, applying the linear wave dispersion relation:

$$c^2 = \frac{g}{k}\tanh(kh) \;\Leftrightarrow\; h = \frac{\lambda}{2\pi}\tanh^{-1}\left(\frac{2\pi c^2}{\lambda g}\right) \tag{5}$$

where $k = \frac{2\pi}{\lambda}$ and g is the gravitational acceleration.

3.1.3. Wavelength adapted recursion

The method presented in this study integrates both spatial and temporal information from all time series within the dataset. The depth estimation at a specific point depends on the size of the correlation window used. A wider correlation window yields a smoother final bathymetry, reducing noise, but it might miss smaller-scale morphological features. Conversely, the correlation window should include at least one complete wavelength of the wavefield. In other words, it is not possible to extract wavelengths larger than the size of the correlation window itself. To address this limitation, the depth estimation process is performed twice to optimise the capture of small-scale morphologies without being constrained by wavelength limitations. In the first iteration, a wide correlation window is used to estimate the wavelength at each point. Then, in the second iteration, the correlation window is adapted to be 2 times the previously estimated wavelength, enabling a more precise extraction of small-scale morphological features.

3.2. Sky-glint surface elevation analysis

3.2.1. Deriving the surface elevation anomaly

Almar et al. (2021a) propose that the optical signal detected by the satellite serves as a proxy for the slope of the free surface elevation. Based on this hypothesis, they developed a methodology called surface elevation analysis, which is designed to extract surface elevation anomalies from UAV videos. The different steps involved in the surface elevation analysis are summarised in this section. After gathering of all the required geometrical information of the acquisition, a linear regression model generates the transfer function linking the pixel intensity to the surface slope. In the case of the Saint-Louis acquisition, the required geometrical information are azimuth and zenith angles, satellite and pixel positions. Azimuth and zenith angles are extracted

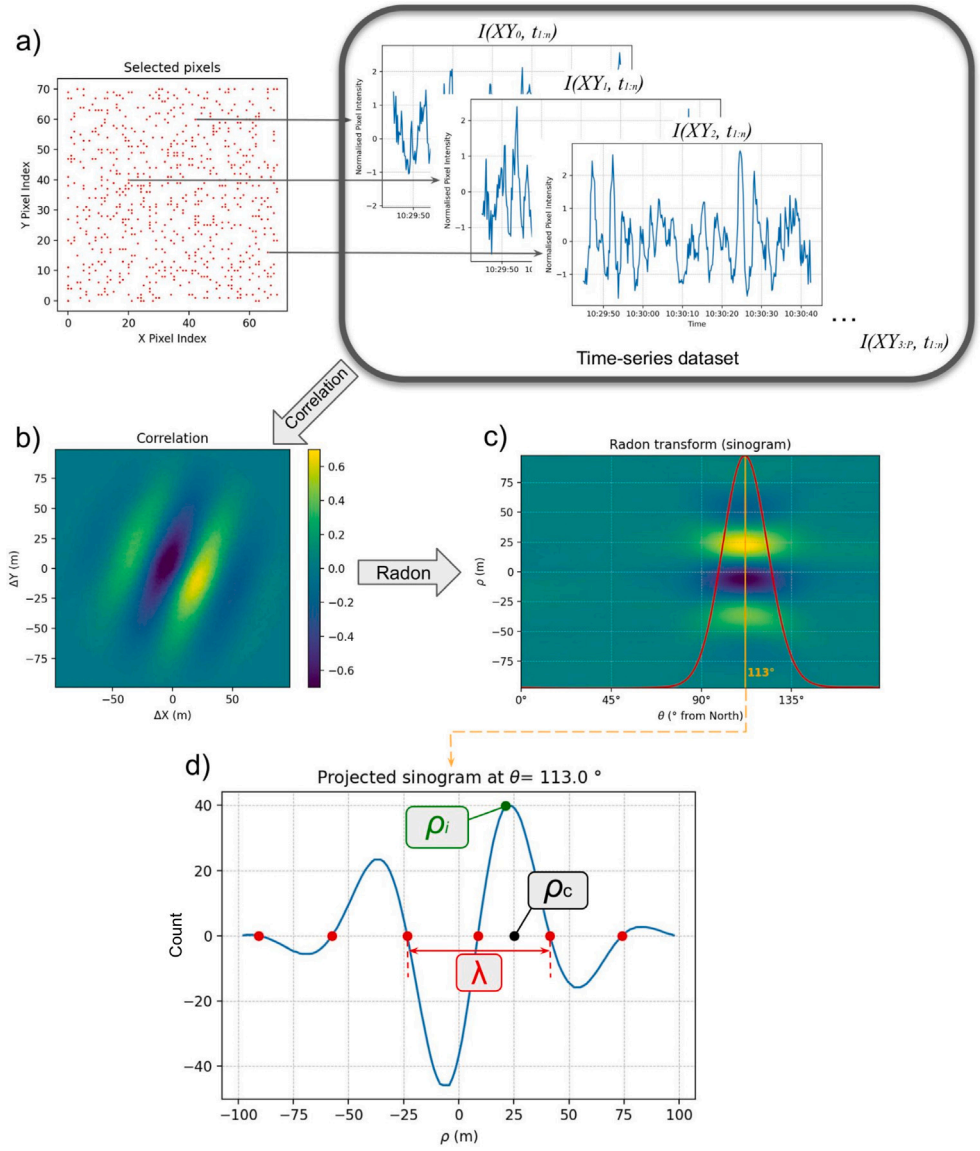

Fig. 4. (a) Random selection of 15 percents of the pixels within the correlation window and extraction of the resulting pixel time-series dataset. (b) Correlation matrix computed from the time-series dataset after application of a Gaussian mask. (c) Resulting sinogram from the Radon Transform of the correlation matrix. The solid red line refers to the variance of the sinogram with respect to the rotational angle. The maximum variance indicate the wave propagation direction. In this case, highlighted by the solid orange line, the wavefield propagates in the direction 113 ° from North. (d) Sinogram projected in the wave propagation direction. Wavelength is computed based on the 0 crossings of the projected sinogram. The maximum peak gives an initial wave displacement ρ_i which is linked to the wavelength as a refinement ρ_c.

directly from the metadata associated to the video (see Fig. 1b). Roll angle is considered negligible. The location (x_0, y_0, z_0,) of the satellite is computed assuming an altitude of 535 km as it is the only altitude value available on the official Jilin website (Jilin-1GF03C, 2024). The pixel locations are determined through georeferencing, achieved after correction and co-registration of each frame. A 2D FFT band-pass filter with high cut off period set at 40 m and low cut off period set to 300 m is applied to the surface slope derived from the transfer function. Slopes are ten projected into polar coordinates with the satellite as origin. The polar grid is chosen with a radial resolution equal to the acquisition's spatial resolution of 1.41 m. We set the polar beams to be equally spaced in angle, originating from the satellite's position and covering all the pixels of the acquisition, ensuring that each pixel is covered by nearly one beam. The slopes are then integrated along the polar beams to derive the surface elevation. Non pertinent signal is removed by a band-pass filter in the polar beam axis over the wavelength range of 10 m to 200 m to remove most of the remaining noise after visual inspection.

3.2.2. Relative Azimuth MTF modulation correction

In this section we consider only the correction of the MTF modulation assuming an observed radiance generated by the sky-glint. We apply a correction proportional to $\cos(\alpha)$, where α, the view angle, represents the relative azimuth angle formed between the sensor azimuth view angle (see Fig. 1b) and a wave propagation direction. We intend to correct for every possible wave propagation direction, then $\alpha \in [0°; 90°]$. A wave field propagating perpendicular to the view angle ($\alpha = 90°$) is not observable (Perugini et al., 2019). In contrast, the observed wave field exhibits the highest contrast when propagating in the direction of the sensor view, specifically from the rear or front of the wave ($\alpha = 0°$) (Kudryavtsev et al., 2017; Almar et al., 2019, 2021a). The Radon transform (RT) sinogram of the surface elevation anomaly is divided by the coefficient $\cos(\theta)$, where θ is the angular axis of the RT space ranging from 0° to 180°. In the case of a surface elevation anomaly projected in a polar projection centered on the satellite position, we denote $\alpha \equiv \theta$. However, RT is set to 0 for $\theta = [75°; 105°]$ as around $\theta = 90°$ only noise is retrieved by the

sensor (Perugini et al., 2019). After applying the coefficient to the RT, the surface elevation anomaly is inverted back to the satellite-centered polar space and then projected onto the original Cartesian grid.

3.3. Application of the temporal correlation method to Jilin spaceborne videos

We used the temporal correlation method to estimate bathymetry along the coast of Saint-Louis, Sénégal, using video data from the Jilin satellite captured on April 7, 2022. Firstly, we applied the method to frame stacks derived from the Jilin video, using a fixed correlation window size of 250 m to calculate each bathymetric point on the resulting grid. Secondly, bathymetry was computed from the same video using frame stacks where the correlation window size was dynamically adjusted, set at 2 times the previously computed wavelength for each grid point. Thirdly, we constructed the frame stack using outcomes from the Surface Elevation Analysis of the Jilin satellite video, maintaining a fixed correlation window size of 250 m. All three tests were conducted on an output grid with a resolution of 5 m. The analysis utilised all 288 frames of the dataset, with pixel extraction limited to 1% of the pixels within each frame stack. We applied a band-pass filter to filter out waves with periods outside of the range from 8 to 25 s We imposed a time lag (Δt) of 3 s for the time-series correlation.

4. Results

4.1. Bathymetric estimations from satellite video acquisitions

Qualitatively, the fixed correlation window SDB in Fig. 5a shows a globally good agreement in the water depth transition between the inner shelf and the surf zone. The alongshore averaged first order nearshore slope is recovered, but two problems remain - (1) small scale morphological features such as nearshore sandbars are missing from this estimate - (2) a constant underestimation of water depth remains throughout the cross-shore profile. On the other hand, the wavelength based adapted correlation window SDB is able to capture the nearshore sandbar and present the zero water depth closer to the real water level of −0.48m on the waterline (see Fig. 5b). There are few in-situ measurements available at the Saint-Louis site, the closest recent beach survey was made 3 years before the Jilin acquisition. Then the position of the sandbar is likely to have moved over time, making it difficult to validate the results quantitatively. However, the inner shelf is less prone to the present large depth variation in time. Taking that situation in consideration, we are more interested by minimising the bias of the estimation then other statistical indicator like the RMSE that are more affected by morphology's evolution. Quantitatively both estimates have a bias of less than 1 m, which is in the range of the 1 m vertical resolution of the survey. The bias for the fixed correlation window SDB is 0.96 m, while the bias for the wavelength adapted SDB is 0.98 m.

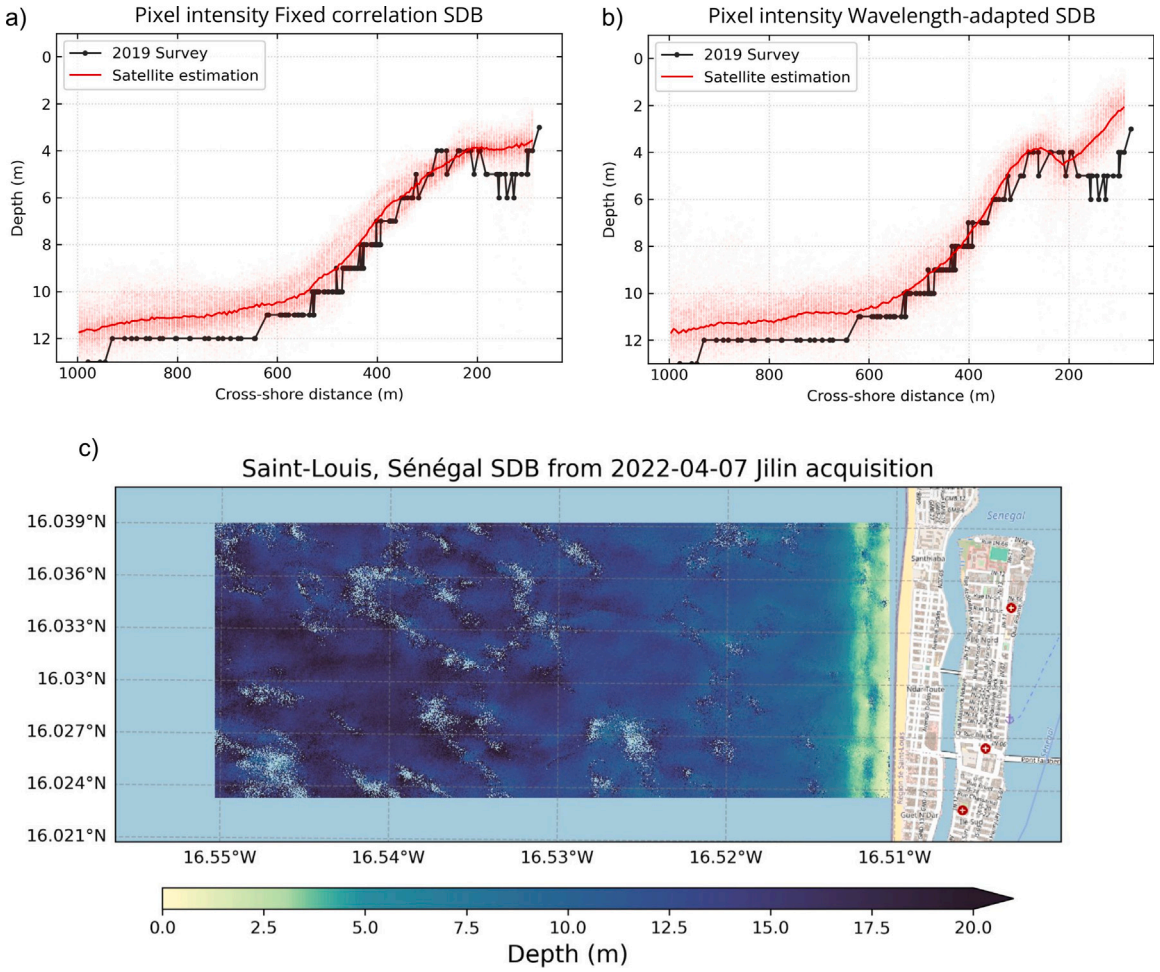

Fig. 5. Satellite Derived Bathymetry (SDB) derived from the Jilin Video (dated 2022-04-07) in Saint-Louis, Sénégal. (a) SDB estimations using a fixed correlation window of 250 m compared to the 2019 in-situ survey. The cross-shore origin is set at the coordinates 338500 on the UTM zone 28N x-axis. b and (c) SDB estimations using a wavelength-adapted correlation window compared to the 2019 in-situ survey. The solid red line depicts the alongshore averaged profile in (b), while (c) displays the resulting grid of the estimation.

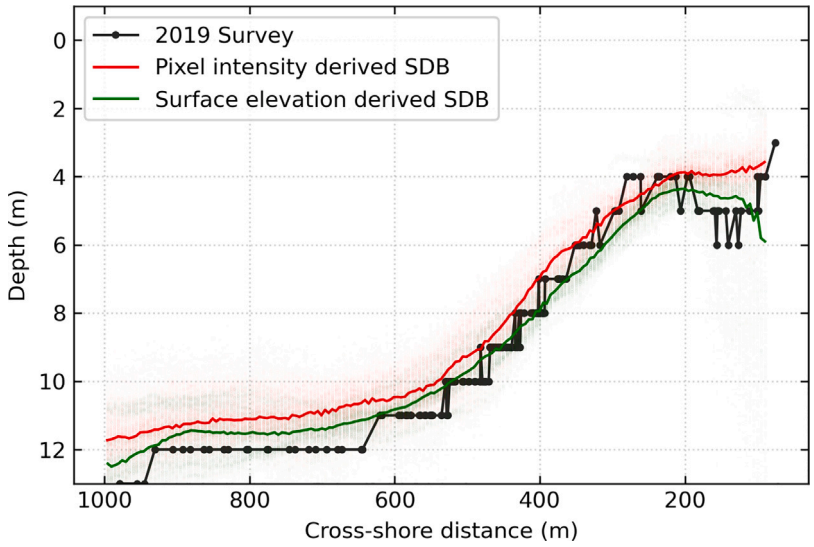

Fig. 6. Comparison of SDB derived from the pixel intensity (in red) and the surface elevation analysis (in green), the 2019 in-situ survey is shown in black. These SDB estimations use a fixed calculation correlation window of 250 m. The solid line represents the alongshore averaged profile of the estimation. The cross-shore origin is set at the coordinates 338500 on the UTM zone 28N x-axis.

4.2. Bathymetric estimations using surface elevation analysis

We computed the SDB from the surface elevation analysis obtained from the Saint-Louis video. To ensure a fair comparison, we maintained consistent parameters and a fixed window size of 250 m for computing SDB from both pixel intensity and surface elevation anomaly. Fig. 6 presents a comparative analysis juxtaposing the resulting SDBs with the in-situ survey conducted three years earlier. As previously mentioned, the pixel intensity-derived SDB exhibits a bias of 0.96 m, while the surface elevation anomaly estimate displays a smaller bias of 0.44 m. It is worth noting that the SDB obtained from the surface elevation anomaly significantly reduces the number of rejected points in the estimation. According to (5), a point cannot be computed if the argument of the inverse hyperbolic tangent function lies outside the domain $[0, 1]$, which is the domain of definition for the inverse hyperbolic tangent function. This situation occurs when c, the celerity or λ, the wavelength are poorly computed due to the presence of a high level of noise in the time series. In total, the pixel intensity-base SDB estimation process discards 428 points, corresponding to 0.3% of the output grid. In contrast, only 2 points are rejected in the surface elevation anomaly-based estimation process, corresponding to 0.0015% of the output grid. Compared to the adapted correlation window SDB, the surface elevation anomaly estimation struggles to fully capture the sandbar, even when an adapted window process is used. This point is discussed in more detail in the Discussion section.

5. Discussion

The temporal correlation method can potentially estimate bathymetry from any video – spaceborne or airborne – or any closely spaced wave time series, extending its use beyond satellite alone. As with other common SDB methods, a few assumptions discussed in this section impose some limitations on this method.

5.1. Temporal correlation method limitations

Depth inversion is primarily dependent on the wave period/length and image resolution, while the wave is observably strongly dependent on the relative angles between the incident waves, the satellite viewing angle and the position of the sun (Bergsma et al., 2019a). Almar et al. (2022) compared spatial and spectral methods with temporal methods for estimating SDB. They concluded that the dimension offering the most information, whether spatial or temporal, should be utilised. For long video sequences with duration longer than one wave period, temporal methods proved to be more accurate. Also the temporal correlation method assumes that a one predominant swell wave is present on the acquisition. The method is only able to determine a single peak wavelength, peak direction and phase celerity of the wave. Multiple swells may lead to a confused correlation matrix, that could be detrimental to discriminate the wave characteristics of only one swell.

According to linear theory limitations, the deep water domain is found when $d > \frac{\lambda}{2}$. In the deep water domain the linear dispersion relation does not hold as the waves do not interact with the bottom. Taking a reasonable limit, the linear dispersion domain is assumed valid for $d < \frac{\lambda}{5}$ (Thuan et al., 2019). Given the offshore conditions at the time of acquisition, where the peak period T_p is 7.4 s, the offshore wavelength is $L = \frac{gT^2}{2\pi} \sim 85$ m. Thus, the deep water limit is approximately at 17 m water depth. On the other hand, the validity of the linear dispersion relation decreases as the wave nonlinearity increases closer to shore, leading to an overestimation of the water depth in the shallow water domain (Bergsma and Almar, 2018). In our study, with an offshore wavelength of 85 m, the shallow water domain begins at a depth of 4.25 m, where the sandbar is located. The SDB presented in this study range from 2 m to 20 m water depth (see Fig. 5c), that is in the range of the theoretical domain of validity of the linear wave-bottom interaction calculated previously. Improvements in depth estimation using non-linear depth inversion methods are expected to lead to improved detection of the sandbar. However, non-linear approaches often require information on incident wave properties, such as wave height and period, which are not available for SDB estimation at sites where in-situ sensors are not deployed.

5.2. Surface elevation analysis contribution and limitation

Throughout this study we have seen the advantage of working with a surface elevation anomaly over working with direct pixel intensity for bathymetry estimation. With the surface elevation anomaly we reduce the noise through filters and resolve the surface elevation by integrating the slope signal. The slope proxy acquired by the sensor is converted thanks to the calculation of the MTF using the sky-glint methodology from Almar et al. (2021a). Also, the relative angle correction stabilise the wavefield acquired through a changing view angle during the acquisition. An illustration of the signal stabilisation can be seen in Fig. 7. It presents a comparative spectral analysis of a 1 km by 1 km

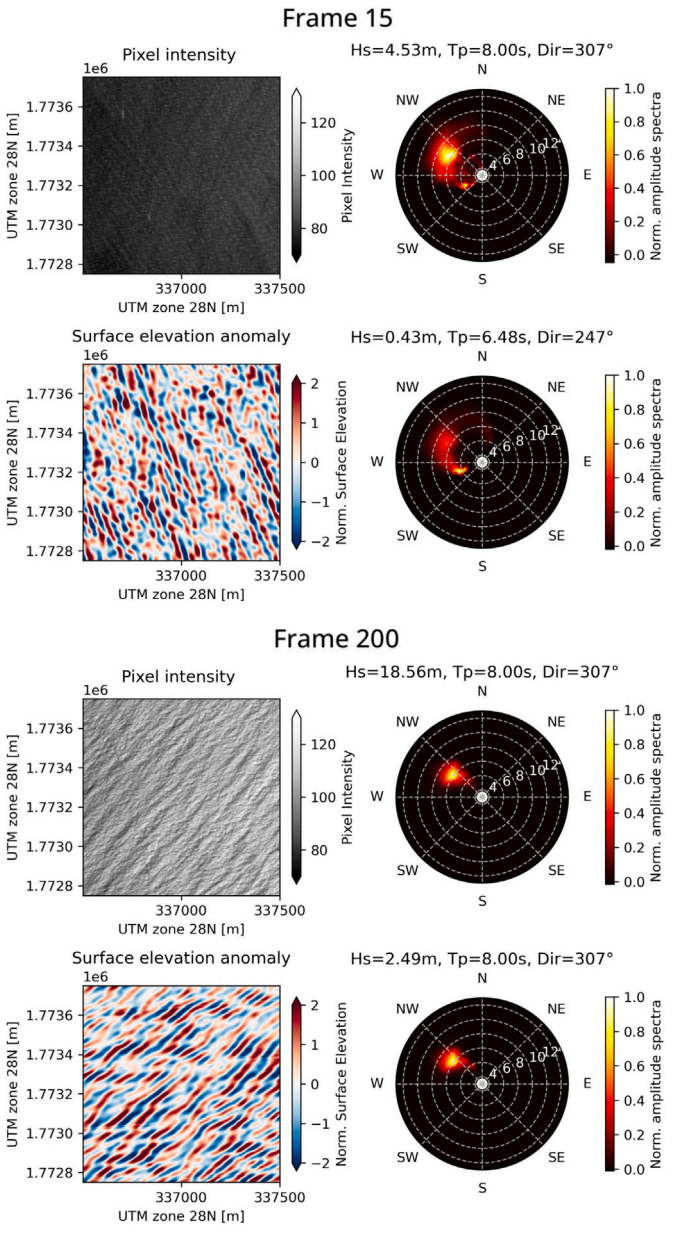

Fig. 7. Pixel intensity and surface elevation anomaly normalised spectrum evolution through the St-Louis Jilin video acquisition. On the normalised spectrum, the radius represent the wave peak period while the angle represents the incident wave direction.

offshore area from the St-Louis video in both pixel intensity (upper line) and surface elevation anomaly (lower line). Examining the pixel intensity spectrum reveals a quick vanishing of a small period (5 s) swell from the South West (230°) due to MTF changes induced by varying view angles. Additionally, the 8s period swell originating from the North West (300°) exhibits energy dispersion over a 50° range from 270° to 320° at the beginning of the acquisition (frame 15). The surface elevation anomaly spectrum demonstrates a more distinct signal separation between the two swell systems, with reduced energy spread. Thanks to the sky-glint related relative azimuth angle correction the South West swell persists for a more extended duration.

Still in the surface elevation anomaly, we observe a fading of the South West swell towards the end of the acquisition, attributed to the MTF causing brightness fluctuations induced by sun glitter. A similar modulation effect occurs at the beginning of the acquisition with the North West swell. In this study, our surface elevation analysis is conducted using the sky-glint methodology. However, given the acquisition configuration featuring intense sun glitter, an analysis incorporating a sun-glint methodology could be applied as well and might correct these modulations. When the sky-glint is the main contribution to the observed radiance, the relative satellite azimuth view angle is the important geometric parameter, as assumed in our study. Its relative orientation to the wave crest modulates the brightness response, with the wave perpendicular to the view angle exhibiting less brightness modulation. On the other hand, when the sun-glint is the main contribution to the observed radiance, the important azimuth angle is that of the bisector between the sun and the satellite. In such situation, the sun and satellite emitter-receptor bi-static configuration can be simplified into an equivalent monostatic configuration, where the equivalent view angle is that of the bisector between the sun and the satellite (Jackson and Alpers, 2010; Rascle et al., 2018). The exact comparison between sky-glint and sun-glint methodologies, with their respective view angles, is left for further study.

As a result, it can be asserted that surface elevation anomaly provides a more faithful representation of actual wave dynamics before the breaking point compared to sensor-acquired data. Then SDB derived from it presents less bias and more stable results as a lot of different noise source where corrected or removed. However, one issue intrinsically associated to the surface elevation analysis remains, accurate estimation of surface elevation anomaly encounters difficulties in the surfzone. The sky-glint effect is present in the MTF function before the breaking point of the waves. On the other hand after the breaking point, namely in the surfzone, the isotropic light scattering generated by the white foam is the governing mechanism of the MTF, preventing the sky-glint effect to occur. This sudden change in the governing mechanism of the MTF leads to incorrect estimations of the surface elevation anomaly after the breaking point. Consequently, the methodology proposed by Almar et al. (2021a) may not be applicable in surfzone regions with a high proportion of wave rollers (or white foam). Therefore, while using pixel intensities introduces a higher estimation error, caution is necessary when computing SDB where the input dataset is a sky-glint derived surface elevation anomaly in the presence of foam in the surfzone. A composite approach that integrates both methods could be considered.

5.3. Spaceborne videos: general considerations and limitations

High resolution videos acquired by Jilin satellite present advantageous characteristics for missions designed to study hydrodynamic conditions and wave kinematics in the coastal zone. The 5 Hz push-frame acquisition lasting up to the minute could constitute a well suited dataset for tracking the different waves ranging from 3 to 25 s and their propagation over a wide area (greater than 100 s of km^2) (Almar et al., 2022). However, the Jilin sensor shoots videos at an 8-bit depth, which is particularly detrimental for wave acquisition. A sensitivity analysis of the time-series band-pass filter (not presented in this study) revealed that the error in bathymetry estimation increased significantly for low cut-off periods shorter than 8 s. The low Signal-to-Noise Ratio (SNR) in the Jilin 8-bit depth acquisition necessitates setting a relatively high value for the low cut-off period to remove noise. It is known that wave period influences bottom estimation predictions; shorter wave periods result in shorter local wavelengths and better adaptation to the underlying seafloor (Thuan et al., 2019; Santos et al., 2022). In shallow water, there is a trade-off in setting the low cut-off period between minimising the estimation error from residual noise after filtering and the error induced by not tracking shorter waves. Additionally, the low SNR of the acquisition introduces a primary source of error when deriving the optical model with sky-glint. Therefore, a 12-bit depth acquisition would be preferable for such acquisitions.

Finally, it is worth mentioning the need for frequent in-situ measurements, which are essential for the validations of new methodologies in bathymetry estimations using remotely sensed data. Despite advances in remote sensing technologies, the unique challenges of bathymetric measurements remain unresolved, underlining the importance

of accurate in-situ data. This study highlights the persistent difficulties associated with scarce in-situ bathymetric measurements, underlining in particular the urgent need to find alternative solutions such as satellites (Turner et al., 2021). Satellite derived estimates are a potentially viable solution to provide a good and accurate means of sensing large areas where bathymetric measurements are not available (Almar et al., 2021b).

6. Conclusion

This study details the temporal correlation method and recent enhancements for estimating nearshore bathymetry from short (around 1 min) spaceborne videos. The method involves correlating pixel intensity time series shifted in time and space, extracted from a correlation window within a stack of frames. The resulting correlation is analysed through Radon transform space to infer wave characteristics (celerity, and wavelength) for depth estimation. Applied to a one-minute Jilin satellite video (1.4-meter resolution) along the coast of Saint-Louis in Senegal, the SDB derived from the Jilin video using the temporal correlation method indicates a bias of 0.97 m within the first 2 km of the cross-shore profile (depth ranging from 0 to 16 m), compared to an in-situ survey conducted three years prior to the video acquisition. A notable improvement involves the wavelength-based adaptation of the correlation window at each point of the output grid. The adaptive correlation window process proves effective in capturing beach features, exemplified by the identification of the submerged sandbar on the Saint-Louis beach. Furthermore, utilising the surface elevation anomaly derived from pixel intensity as input reduces the SDB estimation bias to 0.44 m. This results highlight the potential application of the temporal correlation method on future Earth observation satellite missions that will capture image sequences (or videos) such as CO3D (CNES/Airbus). While the present study focuses on spaceborne videos, the temporal correlation method's versatility invites further exploration and validation using alternate sources such as camera-mounted or Unmanned Aerial Vehicle (UAV) recordings.

CRediT authorship contribution statement

Adrien N. Klotz: Writing – original draft, Methodology, Investigation, Formal analysis, Conceptualization. **Rafael Almar:** Writing – review & editing, Methodology, Conceptualization. **Yohan Quenet:** Writing – review & editing, Methodology. **Erwin W.J. Bergsma:** Writing – review & editing, Funding acquisition, Conceptualization. **David Youssefi:** Data curation. **Stephanie Artigues:** Writing – review & editing, Data curation. **Nicolas Rascle:** Writing – review & editing. **Boubou Aldiouma Sy:** Writing – review & editing. **Abdoulaye Ndour:** Writing – review & editing.

Declaration of competing interest

The authors declare that they have no known competing financial interests or personal relationships that could have appeared to influence the work reported in this paper.

Data availability

Data will be made available on request.

Acknowledgments

This research was supported by the ANR-22-ASTR-0013-01 GLOBCOASTS project and the Coastal Protection Project in Saint-Louis (PPCS), funded by the Senegalese ADM and the French AFD. The authors would also like to thank the three anonymous reviewers for their valuable comments and feedback which greatly helped to improve the quality of the manuscript.

References

Abessolo, G.O., Almar, R., Bonou, F., Bergsma, E., 2020. Error proxies in video-based depth inversion: Temporal celerity estimation. J. Coast. Res. 95 (SI), 1101–1105, https://doi.org/10.2112/SI95-214.1.

Abileah, R., 2006. Mapping shallow water depth from satellite. In: Proceedings of the ASPRS Annual Conference. Reno, Nevada, ASPRS Bethesda, ML, pp. 1–7, https://www.asprs.org/a/publications/proceedings/reno2006/0001.pdf.

Almar, R., Bergsma, E.W.J., Brodie, K.L., Bak, A.S., Artigues, S., Lemai-Chenevier, S., Cesbron, G., Delvit, J.-M., 2022. Coastal topo-bathymetry from a single-pass satellite video: Insights in space-videos for coastal monitoring at Duck Beach (NC, USA). Remote Sens. 14 (7), https://doi.org/10.3390/rs14071529.

Almar, R., Bergsma, E.W.J., Catalan, P.A., Cienfuegos, R., Suarez, L., Lucero, F., Lerma, A.N., Desmazes, F., Perugini, E., Palmsten, M.L., Chickadel, C., 2021a. Sea state from single optical images: A methodology to derive wind-generated ocean waves from cameras, drones and satellites. Remote Sens. 13 (4), https://doi.org/10.3390/rs13040679.

Almar, R., Bergsma, E.W., Maisongrande, P., de Almeida, L.P.M., 2019. Wave-derived coastal bathymetry from satellite video imagery: A showcase with Pleiades persistent mode. Remote Sens. Environ. 231, 111263, https://doi.org/10.1016/j.rse.2019.111263.

Almar, R., Bergsma, E.W.J., Thoumyre, G., Baba, M.W., Cesbron, G., Daly, C., Garlan, T., Lifermann, A., 2021b. Global satellite-Based Coastal bathymetry from waves. Remote Sens. 13 (22), https://doi.org/10.3390/rs13224628.

Almar, R., Bergsma, E.W., Thoumyre, G., Lemai-Chenevier, S., Loyer, S., Artigues, S., Salles, G., Garlan, T., Lifermann, A., 2024. Satellite-derived bathymetry from correlation of Sentinel-2 spectral bands to derive wave kinematics: Qualification of Sentinel-2 S2Shores estimates with hydrographic standards. Coast. Eng. 189, 104458, https://doi.org/10.1016/j.coastaleng.2024.104458.

Almar, R., Bonneton, P., Senechal, N., Roelvink, D., 2009. Wave celerity from video imaging: A new method. In: Coastal Engineering 2008: (in 5 Volumes). World Scientific, pp. 661–673, https://doi.org/10.1142/9789814277426_0056.

Anfuso, G., Postacchini, M., Di Luccio, D., Benassai, G., 2021. Coastal sensitivity/vulnerability characterization and adaptation strategies: A review. J. Mar. Sci. Eng. 9 (1), https://doi.org/10.3390/jmse9010072.

Angnuureng, D.B., Jayson-Quashigah, P.-N., Almar, R., Stieglitz, T.C., Anthony, E.J., Aheto, D.W., Appeaning Addo, K., 2020. Application of shore-based video and unmanned aerial vehicles (drones): Complementary tools for beach studies. Remote Sens. 12 (3), https://doi.org/10.3390/rs12030394.

Bergsma, E.W., Almar, R., 2018. Video-based depth inversion techniques, a method comparison with synthetic cases. Coast. Eng. 138, 199–209, https://doi.org/10.1016/j.coastaleng.2018.04.025.

Bergsma, E.W.J., Almar, R., Maisongrande, P., 2019a. Radon-augmented Sentinel-2 satellite imagery to derive wave-patterns and regional bathymetry. Remote Sens. 11 (16), https://doi.org/10.3390/rs11161918.

Bergsma, E.W., Almar, R., Melo de Almeida, L.P., Sall, M., 2019b. On the operational use of UAVs for video-derived bathymetry. Coast. Eng. 152, 103527, https://doi.org/10.1016/j.coastaleng.2019.103527.

Bergsma, E.W., Almar, R., Rolland, A., Binet, R., Brodie, K.L., Bak, A.S., 2021. Coastal morphology from space: A showcase of monitoring the topography-bathymetry continuum. Remote Sens. Environ. 261, 112469, https://doi.org/10.1016/j.rse.2021.112469.

Bergsma, E., Conley, D., Davidson, M., O'Hare, T., 2016. Video-based nearshore bathymetry estimation in macro-tidal environments. Mar. Geol. 374, 31–41, https://doi.org/10.1016/j.margeo.2016.02.001.

Bergsma, E.W.J., Conley, D.C., Davidson, M.A., O'Hare, T.J., Almar, R., 2019c. Storm event to seasonal evolution of nearshore bathymetry derived from shore-based video imagery. Remote Sens. 11 (5), https://doi.org/10.3390/rs11050519.

Bian, X., Shao, Y., Zhang, C., Xie, C., Tian, W., 2020. The feasibility of assessing swell-based bathymetry using SAR imagery from orbiting satellites. ISPRS J. Photogramm. Remote Sens. 168, 124–130, https://doi.org/10.1016/j.isprsjprs.2020.08.006.

Brodie, K.L., Bruder, B.L., Slocum, R.K., Spore, N.J., 2019. Simultaneous mapping of coastal topography and bathymetry from a lightweight multicamera UAS. IEEE Trans. Geosci. Remote Sens. 57 (9), 6844–6864, https://doi.org/10.1109/TGRS.2019.2909026.

Brodie, K.L., Palmsten, M.L., Hesser, T.J., Dickhudt, P.J., Raubenheimer, B., Ladner, H., Elgar, S., 2018. Evaluation of video-based linear depth inversion performance and applications using altimeters and hydrographic surveys in a wide range of environmental conditions. Coast. Eng. 136, 147–160, https://doi.org/10.1016/j.coastaleng.2018.01.003.

Catálan, P.A., Haller, M.C., 2008. Remote sensing of breaking wave phase speeds with application to non-linear depth inversions. Coast. Eng. 55 (1), 93–111, https://doi.org/10.1016/j.coastaleng.2007.09.010.

Cesbron, G., Melet, A., Almar, R., Lifermann, A., Tullot, D., Crosnier, L., 2021. Pan-European satellite-Derived Coastal bathymetry—Review, user needs and future services. Front. Mar. Sci. 8, https://doi.org/10.3389/fmars.2021.740830.

Daly, C., Baba, W., Bergsma, E., Thoumyre, G., Almar, R., Garlan, T., 2022. The new era of regional coastal bathymetry from space: A showcase for West Africa using optical Sentinel-2 imagery. Remote Sens. Environ. 278, 113084, https://doi.org/10.1016/j.rse.2022.113084.

Danilo, C., Binet, R., 2013. Bathymetry estimation from wave motion with optical imagery: Influence of acquisition parameters. In: 2013 MTS/IEEE OCEANS. Bergen, pp. 1–5, https://doi.org/10.1109/OCEANS-Bergen.2013.6608068.

de Michele, M., Raucoules, D., Idier, D., Smai, F., Foumelis, M., 2021. Shallow bathymetry from multiple sentinel 2 images via the joint estimation of wave celerity and wavelength. Remote Sens. 13 (11), https://doi.org/10.3390/rs13112149.

Hersbach, H., Bell, B., Berrisford, P., Hirahara, S., Horányi, A., Muñoz-Sabater, J., Nicolas, J., Peubey, C., Radu, R., Schepers, D., Simmons, A., Soci, C., Abdalla, S., Abellan, X., Balsamo, G., Bechtold, P., Biavati, G., Bidlot, J., Bonavita, M., De Chiara, G., Dahlgren, P., Dee, D., Diamantakis, M., Dragani, R., Flemming, J., Forbes, R., Fuentes, M., Geer, A., Haimberger, L., Healy, S., Hogan, R.J., Hólm, E., Janisková, M., Keeley, S., Laloyaux, P., Lopez, P., Lupu, C., Radnoti, G., de Rosnay, P., Rozum, I., Vamborg, F., Villaume, S., Thépaut, J.-N., 2020. The ERA5 global reanalysis. Q. J. R. Meteorol. Soc. 146 (730), 1999–2049, https://doi.org/10.1002/qj.3803.

Holman, R., Bergsma, E.W.J., 2021. Updates to and performance of the cBathy algorithm for estimating nearshore bathymetry from remote sensing imagery. Remote Sens. 13 (19), https://doi.org/10.3390/rs13193996.

Holman, R.A., Brodie, K.L., Spore, N.J., 2017. Surf zone characterization using a small quadcopter: Technical issues and procedures. IEEE Trans. Geosci. Remote Sens. 55 (4), 2017–2027, https://doi.org/10.1109/TGRS.2016.2635120.

Holman, R., Haller, M.C., 2013. Remote sensing of the nearshore. Annu. Rev. Mar. Sci. 5, 95–113, https://doi.org/10.1146/annurev-marine-121211-172408.

Holman, R.A., Lalejini, D.M., Edwards, K., Veeramony, J., 2014. A parametric model for barred equilibrium beach profiles. Coast. Eng. 90, 85–94, https://doi.org/10.1016/j.coastaleng.2014.03.005.

Holman, R., Plant, N., Holland, T., 2013. cBathy: A robust algorithm for estimating nearshore bathymetry. J. Geophys. Res. 118 (5), 2595–2609, https://doi.org/10.1002/jgrc.20199.

Jackson, C.R., Alpers, W., 2010. The role of the critical angle in brightness reversals on sunglint images of the sea surface. J. Geophys. Res.: Oceans 115 (C9), https://doi.org/10.1029/2009JC006037.

Jilin-1GF03C, 2024. Jilin-1GF03C—Chang Guang Satellite Technology Co., Ltd. URL http://www.jl1.cn/EWeb/product_view.aspx?id=745. (Accessed 14 February 2024).

Kudryavtsev, V., Yurovskaya, M., Chapron, B., Collard, F., Donlon, C., 2017. Sun glitter imagery of ocean surface waves. Part 1: Directional spectrum retrieval and validation. J. Geophys. Res.: Oceans 122 (2), 1369–1383, https://doi.org/10.1002/2016JC012425.

Lange, A.M.Z., Fiedler, J.W., Merrifield, M.A., Guza, R.T., 2023. UAV video-based estimates of nearshore bathymetry. Coast. Eng. 185, 104375, https://doi.org/10.1016/j.coastaleng.2023.104375.

Lyard, F.H., Allain, D.J., Cancet, M., Carrère, L., Picot, N., 2021. FES2014 global ocean tide atlas: design and performance. Ocean Sci. 17 (3), 615–649, https://doi.org/10.5194/os-17-615-2021.

Matsuba, Y., Sato, S., 2018. Nearshore bathymetry estimation using UAV. Coast. Eng. J. 60 (1), 51–59, https://doi.org/10.1080/21664250.2018.1436239.

Mudiyanselage, S.D., Wilkinson, B., Abd-Elrahman, A., 2024. Automated high-resolution bathymetry from sentinel-1 SAR images in deeper Nearshore Coastal waters in Eastern Florida. Remote Sens. 16 (1), https://doi.org/10.3390/rs16010001.

Ndour, A., Ba, K., Almar, A., Almeida, P., Sall, M., Diedhiou, P., Floc'h, F., Daly, C., Grandjean, P., Boivin, J.-P., Castelle, B., Marieu, V., Biausque, M., Detandt, G., Folly, S.T., Bonou, F., Capet, X., Garlan, T., Marchesiello, P., Benshila, R., Diaz, H., Bergsma, E., Sadio, M., Sakho, I., Sy, B., 2020. On the natural and anthropogenic drivers of the Senegalese (West Africa) Low Coast evolution: Saint Louis Beach 2016 COASTVAR experiment and 3D modeling of short Term Coastal protection measures. J. Coast. Res. 95 (sp1), 583, https://doi.org/10.2112/SI95-114.1.

Ndour, A., bi, R.A.L., Sadio, M., Degbe, C.G., Diaw, A.T., Oyédé, L.M., Anthony, E.J., Dussouillez, P., Sambou, H., hadji Balla Dièye, E., 2018. Management strategies for coastal erosion problems in West Africa: Analysis, issues, and constraints drawn from the examples of Senegal and Benin. Ocean Coast. Manag. 156, 92–106, https://doi.org/10.1016/j.ocecoaman.2017.09.001.

Oades, E.M., Mulligan, R., Palmsten, M., 2023. Evaluation of nearshore bathymetric inversion algorithms using camera observations and synthetic numerical input of surface waves during storms. Coast. Eng. 184, 104338, https://doi.org/10.1016/j.coastaleng.2023.104338.

Palmsten, M.L., Brodie, K.L., 2022. The Coastal imaging research network (CIRN). Remote Sens. 14 (3), https://doi.org/10.3390/rs14030453.

Pereira, P., Baptista, P., Cunha, T., Silva, P.A., Romão, S., Lafon, V., 2019. Estimation of the nearshore bathymetry from high temporal resolution Sentinel-1A C-band SAR data - A case study. Remote Sens. Environ. 223, 166–178, https://doi.org/10.1016/j.rse.2019.01.003.

Perugini, E., Soldini, L., Palmsten, M.L., Calantoni, J., Brocchini, M., 2019. Linear depth inversion sensitivity to wave viewing angle using synthetic optical video. Coast. Eng. 152, 103535, https://doi.org/10.1016/j.coastaleng.2019.103535.

Plant, N.G., Holland, K.T., Haller, M.C., 2008. Ocean wavenumber estimation from wave-resolving time series imagery. IEEE Trans. Geosci. Remote Sens. 46 (9), 2644–2658, https://doi.org/10.1109/TGRS.2008.919821.

Poupardin, A., Idier, D., de Michele, M., Raucoules, D., 2016. Water depth inversion from a single SPOT-5 dataset. IEEE Trans. Geosci. Remote Sens. 54 (4), 2329–2342, https://doi.org/10.1109/TGRS.2015.2499379.

Radermacher, M., Wengrove, M., van Thiel de Vries, J., Holman, R., 2014. Applicability of video-derived bathymetry estimates to nearshore current model predictions. J. Coast. Res. 70 (sp1), 290–295, https://doi.org/10.2112/SI70-049.1.

Rascle, N., Nouguier, F., Chapron, B., Ocampo-Torres, F.J., 2018. Sunglint images of current gradients at high resolution: Critical angle and directional observing strategy. Remote Sens. Environ. 216, 786–797, https://doi.org/10.1016/j.rse.2018.06.011.

Rodríguez-Padilla, I., Castelle, B., Marieu, V., Morichon, D., 2022. Video-based nearshore bathymetric inversion on a geologically constrained mesotidal beach during storm events. Remote Sens. 14 (16), https://doi.org/10.3390/rs14163850.

Sadio, M., Anthony, E.J., Diaw, A.T., Dussouillez, P., Fleury, J.T., Kane, A., Almar, R., Kestenare, E., 2017. Shoreline changes on the wave-influenced Senegal River Delta, West Africa: The roles of natural processes and human interventions. Water 9 (5), https://doi.org/10.3390/w9050357.

Santos, D., Abreu, T., Silva, P.A., Santos, F., Baptista, P., 2022. Nearshore bathymetry retrieval from wave-based inversion for video imagery. Remote Sens. 14 (9), 2155, https://doi.org/10.3390/rs14092155.

Saylam, K., Hupp, J.R., Averett, A.R., Gutelius, W.F., Gelhar, B.W., 2018. Airborne lidar bathymetry: assessing quality assurance and quality control methods with Leica Chiroptera examples. Int. J. Remote Sens. 39 (8), 2518–2542, https://doi.org/10.1080/01431161.2018.1430916.

Sherwood, C.R., van Dongeren, A., Doyle, J., Hegermiller, C.A., Hsu, T.-J., Kalra, T.S., Olabarrieta, M., Penko, A.M., Rafati, Y., Roelvink, D., van der Lugt, M., Veeramony, J., Warner, J.C., 2022. Modeling the morphodynamics of coastal responses to extreme events: What shape are we in? Annu. Rev. Mar. Sci. 14 (1), 457–492, https://doi.org/10.1146/annurev-marine-032221-090215.

Stockdon, H.F., Holman, R.A., 2000. Estimation of wave phase speed and nearshore bathymetry from video imagery. J. Geophys. Res.: Oceans 105 (C9), 22015–22033, https://doi.org/10.1029/1999JC000124.

Stumpf, R.P., Holderied, K., Sinclair, M., 2003. Determination of water depth with high-resolution satellite imagery over variable bottom types. Limnol. Oceanogr. 48 (1part2), 547–556, https://doi.org/10.4319/lo.2003.48.1_part_2.0547.

Thuan, D.H., Almar, R., Marchesiello, P., Viet, N.T., 2019. Video sensing of nearshore bathymetry evolution with error estimate. J. Mar. Sci. Eng. 7 (7), https://doi.org/10.3390/jmse7070233.

Turner, I.L., Harley, M.D., Almar, R., Bergsma, E.W., 2021. Satellite optical imagery in Coastal Engineering. Coast. Eng. 167, 103919, https://doi.org/10.1016/j.coastaleng.2021.103919.

Vitousek, S., Buscombe, D., Vos, K., Barnard, P.L., Ritchie, A.C., Warrick, J.A., 2023. The future of coastal monitoring through satellite remote sensing. Camb. Prisms: Coast. Futures 1, e10, https://doi.org/10.1017/cft.2022.4.

Wiehle, S., Pleskachevsky, A., Gebhardt, C., 2019. Automatic bathymetry retrieval from SAR images. CEAS Space J. 11 (1), 105–114, https://doi.org/10.1007/s12567-018-0234-4.

Wijnberg, K.M., Kroon, A., 2002. Barred beaches. Geomorphology 48 (1), 103–120, https://doi.org/10.1016/S0169-555X(02)00177-0.

Wilson, G.W., Özkan-Haller, H.T., Holman, R.A., Haller, M.C., Honegger, D.A., Chickadel, C.C., 2014. Surf zone bathymetry and circulation predictions via data assimilation of remote sensing observations. J. Geophys. Res.: Oceans 119 (3), 1993–2016, https://doi.org/10.1002/2013JC009213.

Zhou, G., Li, C., Zhang, D., Liu, D., Zhou, X., Zhan, J., 2021. Overview of underwater transmission characteristics of oceanic LiDAR. IEEE J. Sel. Top. Appl. Earth Obs. Remote Sens. 14, 8144–8159, https://doi.org/10.1109/JSTARS.2021.3100395.